Heliyon 7 (2021) e07601

Contents lists available at ScienceDirect

Heliyon

journal homepage: www.cell.com/heliyon

Research article

Modeling of lattice parameters of cubic perovskite oxides and halides

Yun Zhang *, Xiaojie Xu

North Carolina State University, Raleigh, NC 27695, USA

ARTICLE INFO

Keywords:
Perovskite
Crystal structure
Oxide
Halide
Machine learning

ABSTRACT

Perovskites having the chemical formulae of ABX_3 are promising candidates for various electronic, magnetic, and thermal applications. One of the important structural factors is a (the lattice constant), which represents the unit cell size. The variation in the lattice constant is a combined result of interactions between different ions, determined by valence electrons and ionic radii. The size and stability of unit cells have important influences on structural stabilities, bandgap structures, and therefore performance of materials. To obtain the lattice constant of cubic perovskites without going through experimental efforts such as synthesis and measurements, we construct a model based on Gaussian process regressions for cubic perovskite lattice constant predictions. The model utilizes the number of valence electrons as well as ionic radii of alloying elements as predictors. A total of 149 cubic perovskites containing fluorides, chlorides, and bromides with cation combinations of $A^{1+}B^{2+}$, as well as oxides with cation combinations of $A^{1+}B^{5+}$, $A^{2+}B^{4+}$, and $A^{3+}B^{3+}$ are explored. The model demonstrates good performance in terms of stabilities and accuracy, and thus could be a rapid approach to estimate lattice constants.

1. Introduction

Cubic perovskites, ABX_3, represent large groups of compounds that possess enormous diversities in the stoichiometry, structure, and physiochemical property. Depending on the anion type, cubic perovskites can be divided into two major groups, which are the oxide and halide. Because of differences in the valence of the ions of the halogen and oxygen, other alloying elements' types as well as oxidation states are different, and hence the properties of the materials. The monovalent A-cation will occupy unit cells' central positions, and, the monovalent X-anions and the divalent B-cation will form the $[BX_6]$ octahedra which will occupy corners around the A-cation, in cubic perovskite halides' ideal forms [1]. The monovalent ions (e.g., Li^+, Ag^+, Cs^+, and K^+) and organic ions (NH_4^+) could replace A-cations. The divalent ions (e.g., Sn^{2+}, Mg^{2+}, and Ge^{2+}) could replace B-cations. The halogens (e.g., Cl^-, I^-, F^-, and Br^-) could replace X-anions. In the cubic perovskite oxide, however, A-site and B-site cations' valence states can be flexible as well as exhibit different combinations, including $A^{1+}B^{5+}$, $A^{2+}B^{4+}$, and $A^{3+}B^{3+}$.

With different constituting elements, compounds will have varying properties, which could include magnetoresistance, ferromagnetism, ferroelectricity, superconductivity, and piezoelectricity [2, 3, 4, 5]. These materials are promising candidates in different application fields, e.g., the high temperature superconductor [6, 7, 8, 9, 10, 11, 12, 13, 14], the multiferroic material [15, 16, 17, 18, 19], the magnetoresistor [15, 16, 17, 18, 19], the multiferroic material [20], and the topological insulator. In recent years, the halide perovskite has attracted a great amount of attention in many different areas, e.g., the laser cooling, the water splitting, the light emitting diode, and the solar cell [21, 22, 23].

The crystal structure is the fundamental parameter of a crystalline material, which is described by lattice parameters and atomic positions. Despite the large varieties of ABX_3 cubic perovskites, lattice constants (a) represent unit cell sizes. Ionic radii and the number of valence electrons of alloying elements, have a great influence on lattice parameters. Geometrically, ionic radius that depend on the element types, the valence states, the spin states, and the coordination number, are the most basic factors that determine the lengths of unit cell axes in three directions. The number of valence electrons influences the interatomic bonding and thus the lattice structure. Computational approaches have

* Corresponding author.
E-mail address: yzhang43@ncsu.edu (Y. Zhang).

https://doi.org/10.1016/j.heliyon.2021.e07601
Received 2 October 2020; Received in revised form 10 June 2021; Accepted 14 July 2021

been utilized to simulate the crystal structure and model electronic structures, bandgaps, and magnetic orderings to help understand the structure-property relationship. Density-function-theory-based tools are frequently used, which require, at least, the basic structural parameters of repeat units. As one of the inputs, lattice constant values are mostly acquired using experimental methods that need great amounts of materials synthesis efforts as well as measurements [24]. It also limits exploring the ABX_3 compound that is cubic but has not yet been synthesized. Additionally, first-principle simulations are based on known quantum mechanics, which demand high levels of computational resource and may be susceptible to underestimations or overestimations of the ionic interaction in other complex oxides. Machine learning has been applied for modeling and estimating many physical parameters of interest as well as performance of many materials across various types of systems [25, 26, 27, 28, 29, 30, 31, 32, 33, 34, 35, 36, 37, 38, 39, 40, 41, 42, 43, 44, 45, 46, 47, 48, 49, 50, 51]. We construct a model using Gaussian process regressions in order to conduct predictions of the cubic perovskite lattice constants. The model uses ionic radii as well as the number of valence electrons as predictors. The model demonstrates good performance in terms of stabilities and accuracy, and thus could be a rapid approach to estimate lattice constants. Particularly, by incorporating the number of valence electrons into the descriptor set, the model is able to distinguish the same ion with different structural surroundings based on valence, which enhances the predictive power of the model. Due to enormous choices of alloying elements, predicting the lattice constant accurately and efficiently can benefit researchers by saving great amounts of time and predictions can be used as inputs to theoretical research to possibly help expedite studies.

2. Methodology

The Gaussian process regressions (GPRs) come from nonparametric probabilistic types of models that tend to have decent performance for small data [52]. Let us employ $y = x^T\beta + \varepsilon$ to express a linear regression, where $\varepsilon \sim N\left(0, \sigma^2\right)$. A GPR incorporates the following two items in order to explain the target y: (1) latent variables, expressed as $l(x_i)$, $i = 1, 2, \ldots, n$, of Gaussian processes (GPs), which satisfies $l(x_i)$'s being jointly Gaussian, and (2) basis functions, denoted by b, which project the predictors x into the feature space. Covariances of latent variables will capture smoothness of targets.

A GPR can be characterized by the mean and covariance. Let us employ $k\left(x, x'\right) = \mathrm{Cov}\left[l(x), l\left(x'\right)\right]$ to express the covariance, $m(x) = E(l(x))$ to express the mean, and $y = b(x)^T\beta + l(x)$ to express the GPR. $l(x) \sim GP\left(0, k\left(x, x'\right)\right)$ and $b(x) \in \mathbb{R}^p$. We parameterize $k\left(x, x'\right)$ by employing the hyperparameter expressed as θ, and express it with $k\left(x, x'|\boldsymbol{\theta}\right)$. Various algorithms will estimate β, σ^2, and θ and let one to specify b and k.

In this study, we consider the exponential (Equation (1)), squared exponential (Equation (2)), Matern 5/2 (Equation (3)), rational quadratic (Equation (4)), and Matern 3/2 (Equation (5)) kernels, as well as their automatic relevance determination (ARD) variations (Equations (6), (7), (8), (9), and (10)). We also study the empty (Equation (11)), constant (Equation (12)), linear (Equation (13)), and pure quadratic (Equation (14)) basis functions. In Equations (1)–(14), σ_l expresses the characteristic length scale, σ_f expresses the signal standard deviation, $r = \sqrt{\left(x_i - x_j\right)^T\left(x_i - x_j\right)}$, α expresses the positive scale-mixture parameter, σ_m $(m = 1, 2, \ldots, d$ and d expresses the number of predictors) expresses the separate length scale for each predictor in the ARD kernels whose θ is expressed as $(\log\sigma_1, \ldots, \log\sigma_d, \log\sigma_f)$, B is expressed as $\left(b\left(x_1\right), b\left(x_2\right), \ldots, b\left(x_n\right)\right)^T$, X is expressed as $\left(x_1, x_2, \ldots, x_n\right)^T$, and $X^2 = \begin{pmatrix} x_{11}^2 & x_{12}^2 & \cdots & x_{1d}^2 \\ x_{21}^2 & x_{22}^2 & \cdots & x_{2d}^2 \\ \vdots & \vdots & \vdots & \vdots \\ x_{n1}^2 & x_{n2}^2 & \cdots & x_{nd}^2 \end{pmatrix}$.

$$k\left(x_i, x_j|\theta\right) = \sigma_f^2 e^{-\frac{r}{\sigma_l}} \sim \text{Exponential Kernel} \tag{1}$$

$$k\left(x_i, x_j|\theta\right) = \sigma_f^2 e^{-\frac{1}{2}\frac{\left(x_i - x_j\right)^T\left(x_i - x_j\right)}{\sigma_l^2}} \sim \text{Squared Exponential Kernel} \tag{2}$$

$$k\left(x_i, x_j|\theta\right) = \sigma_f^2\left(1 + \frac{\sqrt{5}r}{\sigma_l} + \frac{5r^2}{3\sigma_l^2}\right)e^{-\frac{\sqrt{5}r}{\sigma_l}} \sim \text{Matern 5/2 Kernel} \tag{3}$$

$$k\left(x_i, x_j|\theta\right) = \sigma_f^2\left(1 + \frac{r^2}{2\alpha\sigma_l^2}\right)^{-\alpha} \sim \text{Rational Quadratic Kernel} \tag{4}$$

$$k\left(x_i, x_j|\theta\right) = \sigma_f^2\left(1 + \frac{\sqrt{3}r}{\sigma_l}\right)e^{-\frac{\sqrt{3}r}{\sigma_l}} \sim \text{Matern 3/2 Kernel} \tag{5}$$

$$k\left(x_i, x_j|\theta\right) = \sigma_f^2 e^{-\sqrt{\sum_{m=1}^{d}\frac{\left(x_{im} - x_{jm}\right)^2}{\sigma_m^2}}} \sim \text{ARD–Exponential Kernel} \tag{6}$$

$$k\left(x_i, x_j|\theta\right) = \sigma_f^2 e^{-\frac{1}{2}\sum_{m=1}^{d}\frac{\left(x_{im} - x_{jm}\right)^2}{\sigma_m^2}} \sim \text{ARD–Squared Exponential Kernel} \tag{7}$$

$$k\left(x_i, x_j|\theta\right) = \sigma_f^2 e^{\left(-\sqrt{5\sum_{m=1}^{d}\frac{\left(x_{im} - x_{jm}\right)^2}{\sigma_m^2}}\right)\left(1 + \sqrt{5\sum_{m=1}^{d}\frac{\left(x_{im} - x_{jm}\right)^2}{\sigma_m^2}} + \frac{5}{3}\sum_{m=1}^{d}\frac{\left(x_{im} - x_{jm}\right)^2}{\sigma_m^2}\right)} \sim \text{ARD–Matern 5/2 Kernel} \tag{8}$$

$$k\left(x_i, x_j|\theta\right) = \sigma_f^2\left(1 + \frac{1}{2\alpha}\sum_{m=1}^{d}\frac{\left(x_{im} - x_{jm}\right)^2}{\sigma_m^2}\right)^{-\alpha} \sim \text{ARD–Rational Quadratic Kernel} \tag{9}$$

$$k\left(x_i, x_j|\theta\right) = \sigma_f^2 e^{\left(-\sqrt{3\sum_{m=1}^{d}\frac{\left(x_{im} - x_{jm}\right)^2}{\sigma_m^2}}\right)\left(1 + \sqrt{3\sum_{m=1}^{d}\frac{\left(x_{im} - x_{jm}\right)^2}{\sigma_m^2}}\right)} \sim \text{ARD–Matern 3/2 Kernel} \tag{10}$$

$$B = Empty\ Matrix \sim \text{Empty Basis Function} \tag{11}$$

$$B = I_{n\times 1} \sim \text{Constant Basis Function} \tag{12}$$

$$B = [1, X] \sim \text{Linear Basis Function} \tag{13}$$

$$B = \left[1, X, X^2\right] \sim \text{Pure Quadratic Basis Function} \tag{14}$$

We use the cross-validation technique as well as the Bayesian optimization utilizing the lower confidence bound (LCB) algorithm in order to make parameter estimations. More technical details can be found in, e.g., [26, 27, 28, 29, 30, 31, 32, 33, 34, 35, 36, 37, 39, 40, 41, 42, 43, 44, 45, 46, 47, 48, 49]. For the cross validation, we employ ten randomized folds (refer to Table 1). For a GPR $(f(x))$, the algorithm will evaluate $y_i = f(x_i)$ based on N_s observations $(x_i$'s) randomly obtained in variable bounds, where N_s denotes the point number utilized for the initial evaluation purpose, and, we employ 4. If the evaluation error is determined, the algorithm will take points randomly until it reaches N_s evaluations that are successful. It will proceed to repeat these following procedures: (a) making updates to $f(x)$ in order to reach the posterior distribution $(Q\left(f|x_i, y_i \text{ for } i = 1, \ldots, n\right))$; (b) locating the point (x), which maximizes $a(x)$–the acquisition function. It will stop after it reaches 200 iterations. $a(x)$ evaluates the goodness of a point based on Q. The LCB acquisition function is designed to examine G that is 2 standard deviations (denoted by $2\sigma_Q$) lower than the posterior mean (denoted by μ_Q) for every observation. That is, $G(x) = \mu_Q(x) - 2\sigma_Q(x)$. Hence, $G(x)$ can be seen as representing objective function's lower confidence envelopes of $2\sigma_Q$. The algorithm of the LCB aims at maximizing $2\sigma_Q(x) - \mu_Q(x)$. We perform Bayesian optimizations across the basis function, the kernel, and σ–the noise standard deviation in order to make minimization of cross-validation errors. Fig. 1 expresses the results. We conduct the likelihood maximization expressed in Equation (15) to make estimations of θ and β, where $K(X, X|\theta)$ is expressed

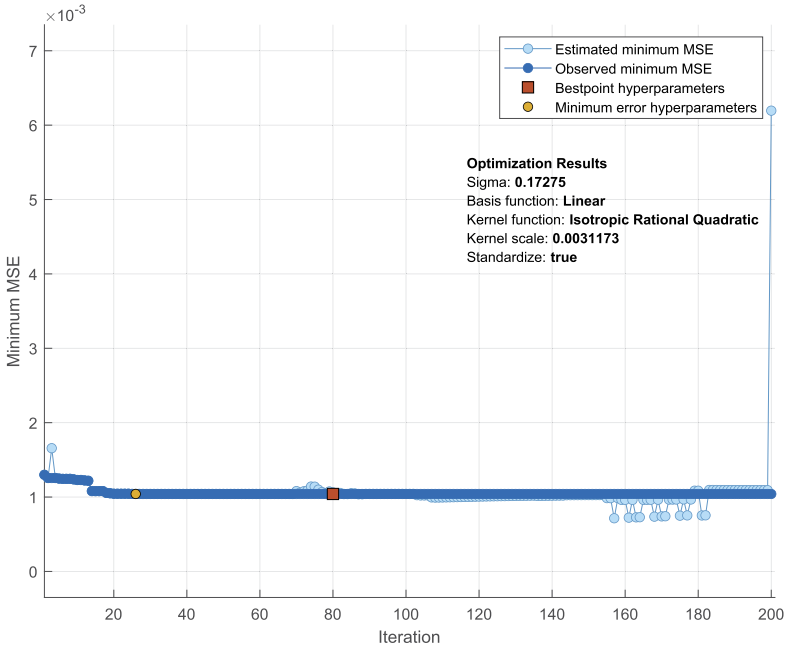

Fig. 1. Bayesian optimization processes.

as $\begin{pmatrix} k(x_1,x_1) & k(x_1,x_2) & \cdots & k(x_1,x_n) \\ k(x_2,x_1) & k(x_2,x_2) & \cdots & k(x_2,x_n) \\ \vdots & \vdots & \vdots & \vdots \\ k(x_n,x_1) & k(x_n,x_2) & \cdots & k(x_n,x_n) \end{pmatrix}$. We make assessments of the model performance using the correlation coefficient (denoted as CC), root mean square error (denoted as RMSE), and mean absolute error (denoted as MAE).

$$\log P\left(y|X,\beta,\theta,\sigma^2\right) = -\frac{1}{2}\{(y-B\beta)^T[K(X,X|\theta)+\sigma^2 I_n]^{-1}(y-B\beta)\} - \frac{n}{2}\log 2\pi - \frac{1}{2}\log\left|K(X,X|\theta)+\sigma^2 I_n\right| \quad (15)$$

3. Dataset

Data analyzed in Table 1 are from [25, 51, 53, 54, 55, 56, 57, 58], which contains fluorides, chlorides, and bromides with cation combinations of $A^{1+}B^{2+}$, as well as oxides with cation combinations of $A^{3+}B^{3+}$, $A^{1+}B^{5+}$, and $A^{2+}B^{4+}$. Descriptors include r_A (Å)–the A-site cation's ionic radii, r_B (Å)–the B-site cation's ionic radii, and r_X (Å)–the X-site anion's ionic radii. Descriptors, V_A, V_B, and V_X, are the numbers of valence electrons of each ion. The targets are a (Å)–experimental lattice constants. It should be noted that V_X is not selected as a predictor in our final model because the value of V_X, or whether the anion is a halogen or an oxygen, is actually dependent on values of V_A and V_B. Fig. 2 plots the data.

4. Result

4.1. Model specification

As can be seen in Fig. 1, the GPR model is specified through the linear basis function and the isotropic rational quadratic kernel, and, the predictors are standardized. The final GPR model is arrived at according to the following procedures. First, we construct the models GPR.CV Fi ($i = 1, 2, ..., 10$), employing samples corresponding to CV Fj's ($j \neq i$) listed in Table 1. There, "CV" expresses "cross-validation" and "F" expresses "fold." Second, every GPR.CV Fi is employ for scoring samples 1–145. Finally, averages of predictions from GPR.CV Fi's serve as predictions from the final model. Through this, the final GPR model could cancel out idiosyncratic irregularities across the data's different folds. Detailed model estimates can be seen from Table 2.

4.2. Model performance

The final GPR model's performance can be seen from Table 3. Its CC, RMSE, and MAE are, respectively, 99.87%, 0.02104, and 0.01618 for observations 1–145 in Table 1. These results show high accuracy. Table 3 summarizes performance of existing models in the literature, including the log-linear equation [25] and linear regressions [51, 53], where we observe improvements through the GPR model. Fig. 3 visualizes different predictions, where it can be observed that the GPR model generates predictions closest to the perfect prediction line.

For observations 146–149, there are no experimental a (Å) values. We apply the final GPR model to obtain their predictions and visualize them with those from [25, 51, 53] in Fig. 4.

One can see that our GPR predictions, generally, lie between those from the log-linear equation [25] and linear regressions [51, 53].

4.3. Stability

The sample has the size of 145, and, is relatively small and shows some potential idiosyncratic patterns of irregularities. Estimates of parameters of the models, expressed in Table 2, in this situation are in general stable. Cross-validation results can be seen from Fig. 5, and, performance of the cross-validation can be seen from Table 4. One can observe that the performance is in general stable too. Because of the cross-validation results' general stabilities, we build the final GPR as a model combination. It could cancel out idiosyncratic patterns of irregularities and produce predictions that are more stable, which can be seen from Fig. 3.

5. Conclusion

As a data-driven method, we construct a model using the Gaussian process regressions in order to make predictions of the lattice constants of cubic perovskite ABX_3. The model uses readily-available parameters of constituting elements and presents the statistical relationship among the ionic radii, the valence electrons number, and the lattice constants. The model's stabilities and accuracy are high. Thus, the model has the potential to be a fast tool for robust estimates of the lattice constants. The model applies to various types of ABX_3 perovskites, both oxides

Table 1. Data analyzed and target predictions.

Category	Index	Solids	Predictors						Target: a (Å)					CV Fold
			r_A (Å)	r_B (Å)	r_X (Å)	V_A	V_B	V_X	Exp.	Pred. [53]	Pred. [51]	Pred. [25]	GPR	
A1 + B2 + X3	1	$CsCdF_3$	1.880	0.950	1.285	1	2	7	4.470	4.430	4.475	4.262	4.477	CV F4
	2	$CsCaF_3$	1.880	1.000	1.285	1	2	7	4.523	4.496	4.539	4.313	4.547	CV F10
	3	$CsHgF_3$	1.880	1.020	1.285	1	2	7	4.570	4.523	4.565	4.334	4.582	CV F3
	4	$CsSrF_3$	1.880	1.180	1.285	1	2	7	4.750	4.747	4.781	4.500	4.786	CV F1
	5	$CsEuF_3$	1.880	1.170	1.285	1	2	7	4.780	4.729	4.767	4.489	4.774	CV F3
	6	$CsPbF_3$	1.880	1.190	1.285	1	2	7	4.800	4.575	4.795	4.510	4.801	CV F5
	7	$CsYbF_3$	1.880	1.020	1.285	1	2	7	4.610	4.523	4.565	4.334	4.582	CV F3
	8	$CsCaCl_3$	1.880	1.000	1.790	1	2	7	5.396	5.360	5.391	4.836	5.381	CV F2
	9	$CsCdCl_3$	1.880	0.950	1.790	1	2	7	5.210	5.289	5.321	4.785	5.257	CV F10
	10	$CsPbCl_3$	1.880	1.190	1.790	1	2	7	5.605	5.639	5.667	5.033	5.628	CV F3
	11	$CsHgCl_3$	1.880	1.020	1.790	1	2	7	5.410	5.389	5.420	4.857	5.425	CV F8
	12	$CsEuCl_3$	1.880	1.170	1.790	1	2	7	5.627	5.610	5.637	5.012	5.605	CV F6
	13	$CsTmCl_3$	1.880	1.030	1.790	1	2	7	5.476	5.404	5.406	4.867	5.442	CV F7
	14	$CsYbCl_3$	1.880	1.020	1.790	1	2	7	5.437	5.389	5.420	4.857	5.425	CV F2
	15	$CsPbBr_3$	1.880	1.190	1.950	1	2	7	5.874	5.921	5.941	5.199	5.879	CV F6
	16	$RbZnF_3$	1.720	0.740	1.285	1	2	7	4.122	4.102	4.143	3.878	4.120	CV F4
	17	$RbCoF_3$	1.720	0.745	1.285	1	2	7	4.141	4.108	4.143	3.884	4.128	CV F7
	18	$RbVF_3$	1.720	0.790	1.285	1	2	7	4.170	4.165	4.203	3.930	4.187	CV F7
	19	$RbFeF_3$	1.720	0.780	1.285	1	2	7	4.174	4.152	4.191	3.920	4.174	CV F9
	20	$RbMnF_3$	1.720	0.830	1.285	1	2	7	4.240	4.215	4.252	3.972	4.246	CV F7
	21	$RbCdF_3$	1.720	0.950	1.285	1	2	7	4.398	4.373	4.405	4.096	4.398	CV F1
	22	$RbCaF_3$	1.720	1.000	1.285	1	2	7	4.452	4.440	4.471	4.148	4.463	CV F6
	23	$RbHgF_3$	1.720	1.020	1.285	1	2	7	4.470	4.468	4.498	4.168	4.493	CV F10
	24	$RbPdF_3$	1.720	0.860	1.285	1	2	7	4.298	4.254	4.290	4.003	4.292	CV F6
	25	$RbYbF_3$	1.720	1.020	1.285	1	2	7	4.530	4.468	4.498	4.168	4.493	CV F2
	26	$RbPbF_3$	1.720	1.190	1.285	1	2	7	4.790	4.705	4.732	4.344	4.759	CV F2
	27	$KCaF_3$	1.640	1.000	1.285	1	2	7	4.380	–	–	4.065	4.391	CV F5
	28	$KCdF_3$	1.640	0.950	1.285	1	2	7	4.293	4.344	4.341	4.013	4.319	CV F6
	29	$KMgF_3$	1.640	0.720	1.285	1	2	7	3.989	4.046	4.048	3.775	4.020	CV F1
	30	$KNiF_3$	1.640	0.690	1.285	1	2	7	4.013	4.009	4.012	3.744	3.984	CV F4
	31	$KZnF_3$	1.640	0.740	1.285	1	2	7	4.056	4.070	4.072	3.796	4.045	CV F6
	32	$KCoF_3$	1.640	0.745	1.285	1	2	7	4.071	4.077	4.072	3.801	4.052	CV F8
	33	KVF_3	1.640	0.790	1.285	1	2	7	4.100	4.134	4.134	3.847	4.117	CV F1
	34	$KFeF_3$	1.640	0.780	1.285	1	2	7	4.121	4.121	4.121	3.837	4.102	CV F4
	35	$KMnF_3$	1.640	0.830	1.285	1	2	7	4.189	4.185	4.184	3.889	4.184	CV F5
	36	$NaVF_3$	1.390	0.790	1.285	1	2	7	3.940	4.037	3.955	3.588	3.947	CV F9
	37	$NaMgF_3$	1.390	0.720	1.285	1	2	7	3.840	–	–	3.516	3.853	CV F3
	38	$NaZnF_3$	1.390	0.740	1.285	1	2	7	3.880	–	–	3.537	3.882	CV F3
	39	$NaCoF_3$	1.390	0.745	1.285	1	2	7	3.900	–	–	3.542	3.889	CV F1
	40	$AgMgF_3$	1.480	0.720	1.285	1	2	7	3.918	3.982	3.930	3.609	3.938	CV F10
	41	$AgNiF_3$	1.480	0.690	1.285	1	2	7	3.936	3.944	3.892	3.578	3.898	CV F8
	42	$AgZnF_3$	1.480	0.740	1.285	1	2	7	3.972	4.004	3.955	3.630	3.961	CV F5
	43	$AgCoF_3$	1.480	0.745	1.285	1	2	7	3.983	4.013	3.955	3.635	3.967	CV F2
	44	$AgMnF_3$	1.480	0.830	1.285	1	2	7	4.030	4.124	4.072	3.723	4.049	CV F4
	45	$LiBaF_3$	1.610	0.760	1.285	1	2	7	3.992	4.084	3.984	3.785	4.033	CV F8
	46	NH_4ZnF_3	1.800	0.740	1.285	1	2	7	4.115	4.134	4.128	3.961	4.119	CV F7
	47	NH_4CoF_3	1.800	0.745	1.285	1	2	7	4.129	4.140	4.128	3.966	4.127	CV F4
	48	NH_4FeF_3	1.800	0.780	1.285	1	2	7	4.177	4.183	4.176	4.003	4.182	CV F9
	49	NH_4MnF_3	1.800	0.830	1.285	1	2	7	4.241	4.246	4.238	4.054	4.256	CV F1
	50	NH_4MgF_3	1.800	0.720	1.285	1	2	7	4.060	4.110	4.104	3.940	4.088	CV F9
	51	$TlCoF_3$	1.700	0.745	1.285	1	2	7	4.138	4.100	4.133	3.863	4.121	CV F7
	52	$TlFeF_3$	1.700	0.780	1.285	1	2	7	4.188	4.144	4.181	3.899	4.168	CV F4
	53	$TlMnF_3$	1.700	0.830	1.285	1	2	7	4.260	4.208	4.243	3.951	4.240	CV F2
	54	$TlCdF_3$	1.700	0.950	1.285	1	2	7	4.400	4.366	4.396	4.075	4.381	CV F10
	55	$TlPdF_3$	1.700	0.860	1.285	1	2	7	4.301	4.247	4.280	3.982	4.284	CV F3
	56	$TlMnCl_3$	1.700	0.830	1.790	1	2	7	5.020	5.064	5.087	4.474	5.013	CV F9
A1 + B5 + O3	57	$CsIO_3$	1.880	0.950	1.350	1	5	6	4.674	4.539	4.596	4.636	4.667	CV F9
	58	$RbUO_3$	1.720	0.760	1.350	1	5	6	4.323	4.234	4.286	4.248	4.319	CV F6
	59	KUO_3	1.640	0.760	1.350	1	5	6	4.290	4.203	4.218	4.159	4.280	CV F8
	60	$RbPaO_3$	1.720	0.780	1.350	1	5	6	4.368	4.259	4.311	4.270	4.350	CV F2
	61	$KPaO_3$	1.640	0.780	1.350	1	5	6	4.341	4.229	4.243	4.181	4.311	CV F2
	62	$KTaO_3$	1.640	0.640	1.350	1	5	6	3.988	4.053	4.072	4.026	4.020	CV F1
	63	$KNbO_3$	1.640	0.640	1.350	1	5	6	4.007	4.053	4.072	4.026	4.020	CV F8
	64	$NaTaO_3$	1.390	0.640	1.350	1	5	6	3.881	3.952	3.886	3.749	3.889	CV F2
	65	$NaAlO_3$	1.390	0.535	1.350	1	5	6	3.730	3.823	3.762	3.632	3.744	CV F9
	66	$NaWO_3$	1.390	0.620	1.350	1	5	6	3.850	3.927	3.861	3.727	3.860	CV F1
A2 + B4 + O3	67	$BaFeO_3$	1.610	0.585	1.350	2	4	6	3.994	3.975	3.998	4.102	3.995	CV F5
	68	$BaMoO_3$	1.610	0.650	1.350	2	4	6	4.040	4.053	4.068	4.177	4.062	CV F7
	69	$BaNbO_3$	1.610	0.680	1.350	2	4	6	4.080	4.091	4.104	4.212	4.092	CV F7
	70	$BaSnO_3$	1.610	0.690	1.350	2	4	6	4.116	4.103	4.117	4.223	4.111	CV F4
	71	$BaHfO_3$	1.610	0.710	1.350	2	4	6	4.171	4.128	4.141	4.246	4.158	CV F5
	72	$BaZrO_3$	1.610	0.720	1.350	2	4	6	4.193	4.141	4.154	4.258	4.183	CV F5
	73	$BaIrO_3$	1.610	0.625	1.350	2	4	6	4.100	4.023	4.045	4.148	4.048	CV F4
	74	$BaPbO_3$	1.610	0.775	1.350	2	4	6	4.265	4.211	4.229	4.322	4.275	CV F8

Table 1 (*continued*)

Category	Index	Solids	Predictors						Target: a (Å)					CV Fold
			r_A (Å)	r_B (Å)	r_X (Å)	V_A	V_B	V_X	Exp.	Pred. [53]	Pred. [51]	Pred. [25]	GPR	
	75	$BaTbO_3$	1.610	0.760	1.350	2	4	6	4.285	4.192	4.204	4.304	4.258	CV F9
	76	$BaPrO_3$	1.610	0.850	1.350	2	4	6	4.354	4.310	4.319	4.408	4.356	CV F8
	77	$BaCeO_3$	1.610	0.870	1.350	2	4	6	4.397	4.336	4.346	4.432	4.384	CV F5
	78	$BaAmO_3$	1.610	0.850	1.350	2	4	6	4.357	4.310	4.319	4.408	4.356	CV F10
	79	$BaNpO_3$	1.610	0.870	1.350	2	4	6	4.384	4.336	4.346	4.432	4.384	CV F1
	80	$BaUO_3$	1.610	0.890	1.350	2	4	6	4.387	4.363	4.372	4.455	4.413	CV F8
	81	$BaPaO_3$	1.610	0.900	1.350	2	4	6	4.450	4.377	4.386	4.466	4.428	CV F9
	82	$BaThO_3$	1.610	0.940	1.350	2	4	6	4.480	4.431	4.439	4.513	4.486	CV F4
	83	$BaTiO_3$	1.610	0.605	1.350	2	4	6	4.012	3.999	4.021	4.125	4.026	CV F10
	84	$BaRuO_3$	1.610	0.680	1.350	2	4	6	4.050	–	–	4.212	4.092	CV F7
	85	$BaPuO_3$	1.610	0.860	1.350	2	4	6	4.360	–	–	4.420	4.370	CV F10
	86	$SrMnO_3$	1.440	0.530	1.350	2	4	6	3.806	3.838	3.837	3.841	3.817	CV F3
	87	$SrVO_3$	1.440	0.580	1.350	2	4	6	3.890	3.898	3.932	3.899	3.872	CV F6
	88	$SrFeO_3$	1.440	0.585	1.350	2	4	6	3.850	3.904	3.908	3.905	3.878	CV F9
	89	$SrTiO_3$	1.440	0.605	1.350	2	4	6	3.905	3.929	3.932	3.928	3.902	CV F9
	90	$SrTcO_3$	1.440	0.645	1.350	2	4	6	3.949	3.979	3.981	3.975	3.950	CV F4
	91	$SrMoO_3$	1.440	0.650	1.350	2	4	6	3.975	3.985	3.981	3.980	3.956	CV F10
	92	$SrNbO_3$	1.440	0.680	1.350	2	4	6	4.016	4.023	4.018	4.015	3.999	CV F2
	93	$SrSnO_3$	1.440	0.690	1.350	2	4	6	4.034	4.036	4.031	4.027	4.018	CV F6
	94	$SrHfO_3$	1.440	0.710	1.350	2	4	6	4.069	4.062	4.056	4.050	4.063	CV F3
	95	$SrTbO_3$	1.440	0.760	1.350	2	4	6	4.180	4.127	4.121	4.108	4.156	CV F10
	96	$SrAmO_3$	1.440	0.850	1.350	2	4	6	4.230	4.248	4.240	4.212	4.250	CV F8
	97	$SrPuO_3$	1.440	0.860	1.350	2	4	6	4.280	4.261	4.253	4.223	4.265	CV F5
	98	$SrCoO_3$	1.440	0.530	1.350	2	4	6	3.850	3.838	3.837	3.841	3.817	CV F2
	99	$SrZrO_3$	1.440	0.720	1.350	2	4	6	4.104	4.075	4.069	4.061	4.086	CV F10
	100	$SrRuO_3$	1.440	0.680	1.350	2	4	6	3.930	3.927	–	4.015	3.999	CV F8
	101	$SrThO_3$	1.440	0.940	1.350	2	4	6	4.420	–	–	4.316	4.399	CV F1
	102	$CaVO_3$	1.340	0.580	1.350	2	4	6	3.767	3.857	3.838	3.784	3.790	CV F2
	103	$CaHfO_3$	1.340	0.710	1.350	2	4	6	3.990	–	–	3.934	3.977	CV F9
	104	$CaZrO_3$	1.340	0.720	1.350	2	4	6	4.010	–	–	3.946	4.000	CV F1
	105	$CaRuO_3$	1.340	0.680	1.350	2	4	6	3.840	–	–	3.899	3.911	CV F8
	106	$CaSnO_3$	1.340	0.690	1.350	2	4	6	3.950	–	–	3.911	3.931	CV F7
	107	$CaTiO_3$	1.340	0.605	1.350	2	4	6	3.840	3.888	3.838	3.813	3.825	CV F4
A3 + B3 + O3	108	$EuTiO_3$	1.230	0.670	1.350	3	3	6	3.905	3.927	3.889	3.801	3.877	CV F5
	109	$EuAlO_3$	1.230	0.535	1.350	3	3	6	3.725	3.755	3.724	3.643	3.718	CV F5
	110	$EuCrO_3$	1.230	0.615	1.350	3	3	6	3.803	3.856	3.824	3.736	3.809	CV F10
	111	$EuFeO_3$	1.230	0.645	1.350	3	3	6	3.836	3.894	3.856	3.771	3.841	CV F3
	112	$EuGaO_3$	1.230	0.620	1.350	3	3	6	3.840	–	–	3.742	3.814	CV F5
	113	$EuInO_3$	1.230	0.800	1.350	3	3	6	4.030	–	–	3.593	4.044	CV F1
	114	$CeAlO_3$	1.340	0.535	1.350	3	3	6	3.772	3.801	3.757	3.771	3.769	CV F6
	115	$GdAlO_3$	1.220	0.535	1.350	3	3	6	3.710	3.750	3.719	3.631	3.708	CV F4
	116	$GdCrO_3$	1.220	0.615	1.350	3	3	6	3.795	3.852	3.819	3.725	3.799	CV F2
	117	$GdFeO_3$	1.220	0.645	1.350	3	3	6	3.820	3.890	3.851	3.760	3.833	CV F6
	118	$LaAlO_3$	1.360	0.535	1.350	3	3	6	3.778	3.810	3.768	3.795	3.777	CV F7
	119	$LaCrO_3$	1.360	0.615	1.350	3	3	6	3.874	3.909	3.866	3.888	3.877	CV F7
	120	$LaFeO_3$	1.360	0.645	1.350	3	3	6	3.920	3.947	3.898	3.923	3.910	CV F3
	121	$LaGaO_3$	1.360	0.620	1.350	3	3	6	3.874	3.915	3.866	3.894	3.883	CV F2
	122	$LaRhO_3$	1.360	0.665	1.350	3	3	6	3.940	3.972	3.930	3.947	3.935	CV F4
	123	$LaTiO_3$	1.360	0.670	1.350	3	3	6	3.920	3.979	3.930	3.953	3.942	CV F2
	124	$LaVO_3$	1.360	0.640	1.350	3	3	6	3.910	3.940	3.891	3.917	3.905	CV F7
	125	$LaInO_3$	1.360	0.800	1.350	3	3	6	4.110	–	–	4.105	4.128	CV F8
	126	$NdAlO_3$	1.270	0.535	1.350	3	3	6	3.752	3.772	3.740	3.689	3.748	CV F6
	127	$NdGaO_3$	1.270	0.620	1.350	3	3	6	3.860	–	–	3.789	3.842	CV F3
	128	$NdInO_3$	1.270	0.800	1.350	3	3	6	4.070	–	–	3.999	4.071	CV F3
	129	$NdCoO_3$	1.270	0.545	1.350	3	3	6	3.777	3.784	3.753	3.701	3.764	CV F5
	130	$NdCrO_3$	1.270	0.615	1.350	3	3	6	3.835	3.872	3.840	3.783	3.838	CV F5
	131	$NdFeO_3$	1.270	0.645	1.350	3	3	6	3.870	3.910	3.872	3.818	3.861	CV F9
	132	$NdMnO_3$	1.270	0.645	1.350	3	3	6	3.800	3.910	3.872	3.818	3.861	CV F6
	133	$PrAlO_3$	1.300	0.535	1.350	3	3	6	3.757	3.784	3.746	3.725	3.758	CV F6
	134	$PrCrO_3$	1.300	0.615	1.350	3	3	6	3.852	3.884	3.845	3.818	3.849	CV F5
	135	$PrFeO_3$	1.300	0.645	1.350	3	3	6	3.887	3.923	3.877	3.853	3.871	CV F6
	136	$PrGaO_3$	1.300	0.620	1.350	3	3	6	3.863	3.891	3.845	3.824	3.853	CV F10
	137	$PrMnO_3$	1.300	0.645	1.350	3	3	6	3.820	3.923	3.877	3.853	3.871	CV F4
	138	$PrVO_3$	1.300	0.640	1.350	3	3	6	3.890	3.916	3.871	3.847	3.867	CV F10
	139	$SmAlO_3$	1.240	0.535	1.350	3	3	6	3.734	3.759	3.729	3.654	3.727	CV F7
	140	$SmCoO_3$	1.240	0.545	1.350	3	3	6	3.750	3.771	3.742	3.666	3.743	CV F1
	141	$SmVO_3$	1.240	0.640	1.350	3	3	6	3.890	3.892	3.855	3.777	3.843	CV F8
	142	$SmFeO_3$	1.240	0.645	1.350	3	3	6	3.845	3.898	3.861	3.783	3.848	CV F3
	143	$YAlO_3$	1.200	0.535	1.350	3	3	6	3.680	3.742	3.697	3.608	3.685	CV F1
	144	$YCrO_3$	1.200	0.615	1.350	3	3	6	3.768	3.843	3.798	3.701	3.777	CV F3
	145	$YFeO_3$	1.200	0.645	1.350	3	3	6	3.785	3.882	3.831	3.736	3.815	CV F9
	146	$BiAlO_3$	1.030	0.535	1.350	3	3	6	–	3.723	3.715	3.409	3.556	–
	147	$BiGaO_3$	1.030	0.620	1.350	3	3	6	–	3.834	3.821	3.508	3.677	–
	148	$BiInO_3$	1.030	0.800	1.350	3	3	6	–	4.111	4.193	3.719	3.932	–
	149	$BiScO_3$	1.030	0.745	1.350	3	3	6	–	4.080	3.974	3.654	3.854	–

(*continued on next page*)

Table 1 (*continued*)

Category	Index	Solids	Predictors						Target: a (Å)					CV Fold
			r_A (Å)	r_B (Å)	r_X (Å)	V_A	V_B	V_X	Exp.	Pred. [53]	Pred. [51]	Pred. [25]	GPR	
Minimum			1.030	0.530	1.285	1	2	6	3.680	3.723	3.697	3.409	3.556	–
Mean			1.517	0.755	1.357	1.839	3.034	6.376	4.164	4.176	4.175	4.015	4.153	–
Median			1.480	0.720	1.350	2	3	6	4.050	4.077	4.072	3.940	4.045	–
Std.			0.222	0.163	0.119	0.839	0.962	0.486	0.420	0.413	0.435	0.337	0.420	–
Maximum			1.880	1.190	1.950	3	5	7	5.874	5.921	5.941	5.199	5.879	–
CC w. Exp. a(A)			77.56%	87.05%	70.59%	-53.42%	-29.67%	49.89%	–	99.31%	99.67%	91.18%	99.87%	–

Notes: It should be noted that V_X is not selected as a predictor in our final model because the value of V_X, or whether the anion is a halogen or an oxygen, is actually dependent on values of V_A and V_B. There are no experimental a (Å) values for observations 146–149. For these four samples, their GPR predictions are obtained by applying the final GPR model. Predictions in [25] are based on the log-linear equation and those in [51] and [53] are based on linear regressions.

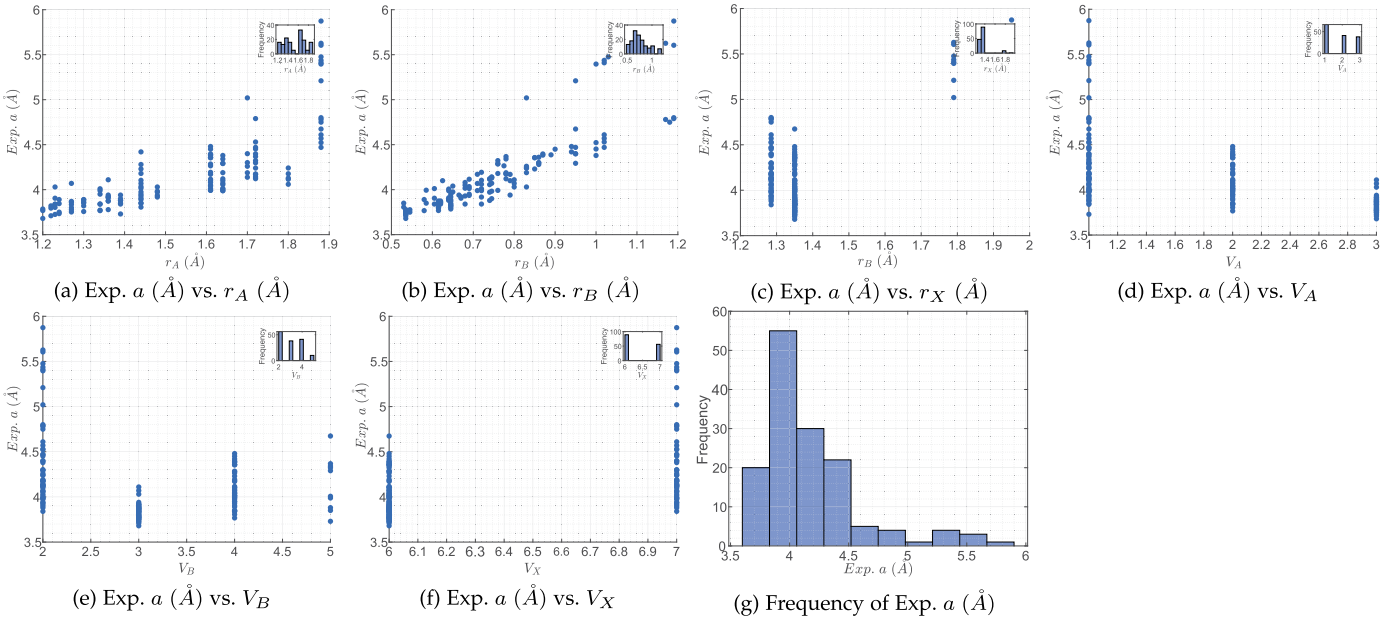

(a) Exp. a (Å) vs. r_A (Å) (b) Exp. a (Å) vs. r_B (Å) (c) Exp. a (Å) vs. r_X (Å) (d) Exp. a (Å) vs. V_A

(e) Exp. a (Å) vs. V_B (f) Exp. a (Å) vs. V_X (g) Frequency of Exp. a (Å)

Fig. 2. Data plots. It should be noted that V_X is not selected as a predictor in our final model because the value of V_X, or whether the anion is a halogen or an oxygen, is actually dependent on values of V_A and V_B. (a) Exp. a (Å) vs. r_A (Å). (b) Exp. a (Å) vs. r_B (Å). (c) Exp. a (Å) vs. r_X (Å). (d) Exp. a (Å) vs. V_A. (e) Exp. a (Å) vs. V_B. (f) Exp. a (Å) vs. V_X. (g) Frequency of Exp. a (Å).

Table 2. Estimates of parameters.

Model		Estimates of parameters									
		σ	β_0	β_1	β_2	β_3	β_4	β_5	σ_l	α	σ_f
Final GPR	GPR.CV F1	0.02548	4.16780	0.13684	0.22871	0.19869	0.02980	0.02068	0.23885	108326.10226	0.02496
	GPR.CV F2	0.02478	4.14943	0.13558	0.22257	0.18297	0.03199	0.01941	0.21371	81074.94010	0.02399
	GPR.CV F3	0.02559	4.15884	0.12722	0.22463	0.19245	0.02843	0.02228	0.26238	140011.28617	0.02736
	GPR.CV F4	0.02355	4.17089	0.13194	0.24320	0.19944	0.02956	0.02300	0.26913	236298.46045	0.02895
	GPR.CV F5	0.02582	4.17061	0.13415	0.23007	0.20057	0.02883	0.02206	0.25052	116079.78874	0.02662
	GPR.CV F6	0.02370	4.15284	0.13151	0.22344	0.17144	0.02896	0.02164	0.22335	63863.24868	0.02816
	GPR.CV F7	0.02534	4.16622	0.13642	0.23617	0.18963	0.03169	0.02280	0.27054	106792.36532	0.02585
	GPR.CV F8	0.02031	4.15864	0.13641	0.24320	0.19050	0.03384	0.02360	0.22511	142151.00534	0.02741
	GPR.CV F9	0.02483	4.16451	0.13185	0.23646	0.19044	0.02771	0.02033	0.23470	133097.23475	0.02710
	GPR.CV F10	0.02432	4.15616	0.13859	0.23156	0.19327	0.03080	0.01997	0.23543	97684.60661	0.02597

Notes: β_0, β_1, β_2, β_3, β_4, and β_5 correspond to the intercept, r_A (Å), r_B (Å), r_X (Å), V_A, and V_B, respectively.

Table 3. Model performance.

	CC	RMSE	$\frac{\text{RMSE}}{\text{Sample Mean}}$	MAE	$\frac{\text{MAE}}{\text{Sample Mean}}$
Pred. [53]	99.31%	0.05476	1.31%	0.04367	1.04%
Pred. [51]	99.67%	0.03541	0.85%	0.02655	0.63%
Pred. [25]	91.18%	0.22609	5.43%	0.16345	3.92%
GPR	99.87%	0.02104	0.51%	0.01618	0.39%

Notes: Results are based on observations 1–145 in Table 1.

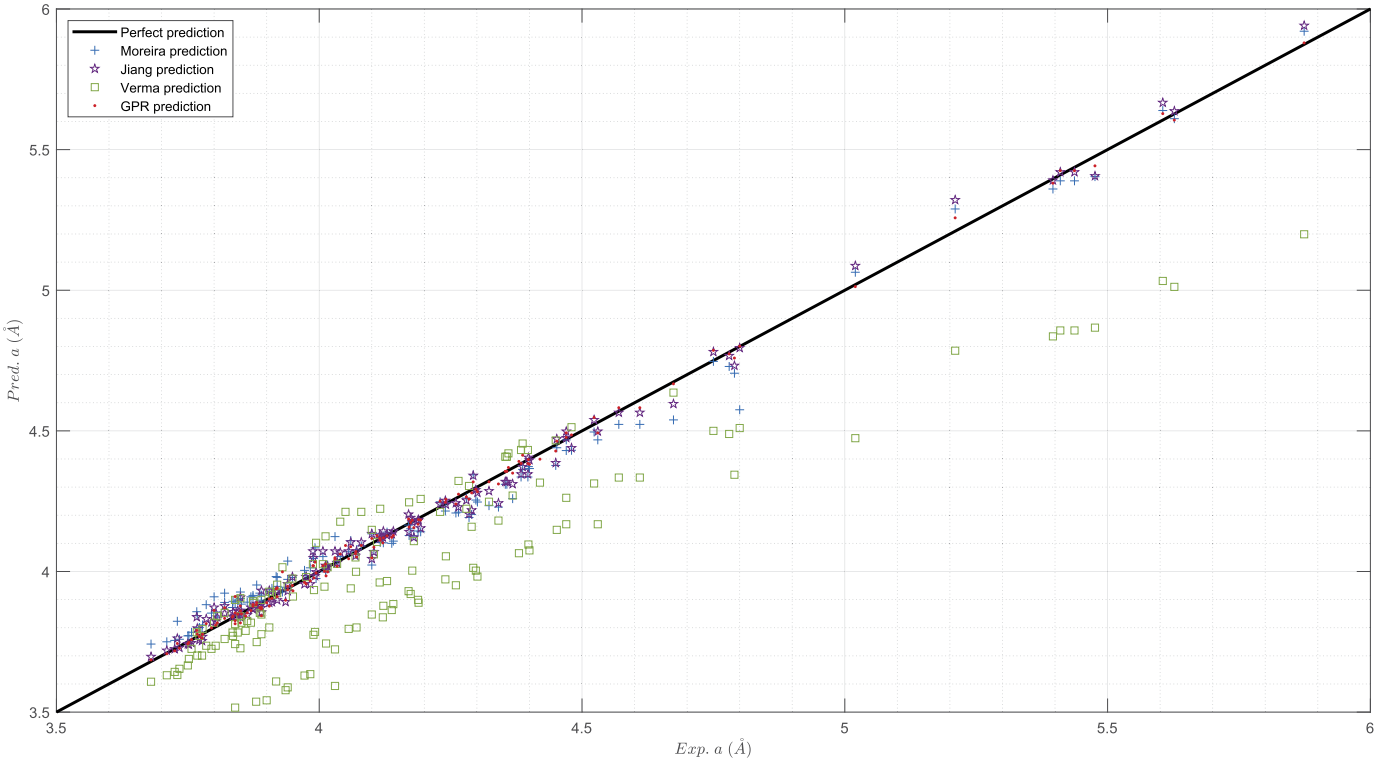

Fig. 3. Experimental lattice constants vs. predicted lattice constants. "Moreira prediction" [53] and "Jiang prediction" [51] are based on linear regression models. "Verma prediction" [25] is based on the log-linear equation. "GPR prediction" shows our result. Results are based on observations 1–145 in Table 1.

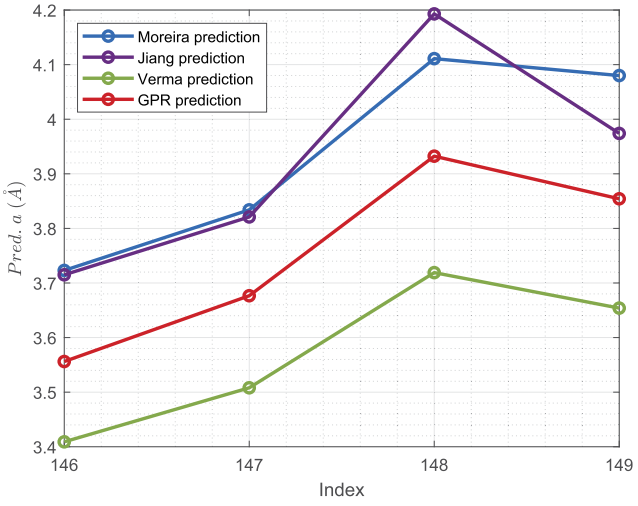

Fig. 4. Predictions of lattice constants. "Moreira prediction" [53] and "Jiang prediction" [51] are based on linear regression models. "Verma prediction" [25] is based on the log-linear equation. "GPR prediction" shows our result. Results are based on observations 146–149 in Table 1.

and halides. Particularly, by incorporating the number of valence electrons into the descriptor set, the model is able to distinguish the same ion with different structural surroundings based on valence, which enhances the predictive power of the model. Compared with many other machine learning methods, the GPR model here is simple and straightforward, without the need of a large number of inputs.

Declarations

Author contribution statement

Yun Zhang: Conceived and designed the experiments; Performed the experiments; Analyzed and interpreted the data; Wrote the paper.

Xiaojie Xu: Performed the experiments; Analyzed and interpreted the data; Contributed reagents, materials, analysis tools or data; Wrote the paper.

Funding statement

This research did not receive any specific grant from funding agencies in the public, commercial, or not-for-profit sectors.

Data availability statement

Data included in article/supplementary material/referenced in article.

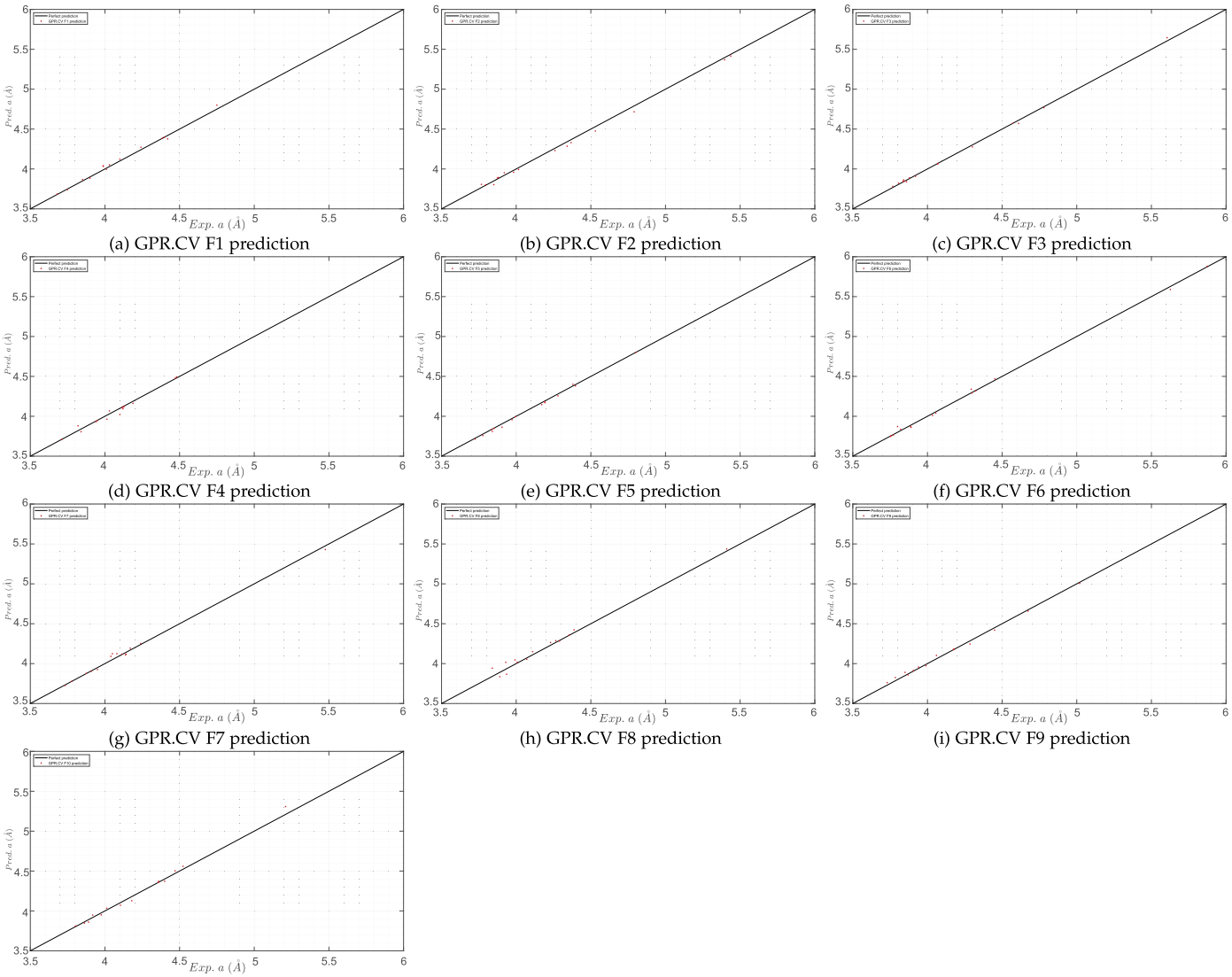

(a) GPR.CV F1 prediction (b) GPR.CV F2 prediction (c) GPR.CV F3 prediction

(d) GPR.CV F4 prediction (e) GPR.CV F5 prediction (f) GPR.CV F6 prediction

(g) GPR.CV F7 prediction (h) GPR.CV F8 prediction (i) GPR.CV F9 prediction

(j) GPR.CV F10 prediction

Fig. 5. Cross validation performance. (a) GPR.CV F1 prediction. (b) GPR.CV F2 prediction. (c) GPR.CV F3 prediction. (d) GPR.CV F4 prediction. (e) GPR.CV F5 prediction. (f) GPR.CV F6 prediction. (g) GPR.CV F7 prediction. (h) GPR.CV F8 prediction. (i) GPR.CV F9 prediction. (j) GPR.CV F10 prediction.

Table 4. Performance of the cross-validation.

	CC		RMSE				MAE			
	Training	Validation	Training	% of Training Sample Mean	Validation	% of Validation Sample Mean	Training	% of Training Sample Mean	Validation	% of Validation Sample Mean
CV F1	99.88%	99.58%	0.021	0.51%	0.029	0.71%	0.016	0.39%	0.024	0.57%
CV F2	99.87%	99.85%	0.021	0.50%	0.038	0.88%	0.015	0.37%	0.033	0.77%
CV F3	99.87%	99.93%	0.021	0.51%	0.019	0.46%	0.016	0.39%	0.015	0.36%
CV F4	99.90%	98.79%	0.019	0.46%	0.033	0.82%	0.015	0.35%	0.024	0.59%
CV F5	99.87%	99.88%	0.022	0.52%	0.019	0.48%	0.017	0.40%	0.016	0.38%
CV F6	99.88%	99.91%	0.019	0.46%	0.027	0.64%	0.015	0.36%	0.020	0.47%
CV F7	99.87%	99.70%	0.021	0.51%	0.033	0.79%	0.016	0.40%	0.025	0.61%
CV F8	99.93%	99.28%	0.016	0.39%	0.049	1.18%	0.012	0.29%	0.040	0.96%
CV F9	99.88%	99.81%	0.021	0.49%	0.026	0.64%	0.016	0.38%	0.023	0.54%
CV F10	99.89%	99.73%	0.020	0.48%	0.038	0.89%	0.016	0.37%	0.030	0.71%
Minimum	99.87%	98.79%	0.016	0.39%	0.019	0.46%	0.012	0.29%	0.015	0.36%
Mean	99.88%	99.65%	0.020	0.48%	0.031	0.75%	0.015	0.37%	0.025	0.60%
Median	99.88%	99.77%	0.021	0.50%	0.031	0.75%	0.016	0.38%	0.024	0.58%
Maximum	99.93%	99.93%	0.022	0.52%	0.049	1.18%	0.017	0.40%	0.040	0.96%
Std	0.02%	0.36%	0.002	0.04%	0.009	0.21%	0.001	0.03%	0.008	0.18%

Declaration of interests statement

The authors declare no conflict of interest.

Additional information

No additional information is available for this paper.

References

[1] M. Johnsson, P. Lemmens, Perovskites and thin films—crystallography and chemistry, J. Phys. Condens. Matter 20 (26) (2008) 264001.

[2] J. Jiang, G. Bradford, S.I. Hossain, M.D. Brown, J. Cooper, E. Miller, Y. Huang, H. Miao, J.A. Parrell, M. White, A. Hunt, S. Sengupta, R. Revur, T. Shen, F. Kametani, U.P. Trociewitz, E.E. Hellstrom, D.C. Larbalestier, High-performance Bi-2212 round wires made with recent powders, IEEE Trans. Appl. Supercond. 29 (5) (2019) 1–5.

[3] T. Shen, E. Bosque, D. Davis, J. Jiang, M. White, K. Zhang, H. Higley, M. Turqueti, Y. Huang, H. Miao, U. Trociewitz, Stable, predictable and training-free operation of superconducting Bi-2212 Rutherford cable racetrack coils at the wire current density of 1000 A/mm^2, Sci. Rep. 9 (1) (2019) 1–9.

[4] H. Song, F. Hunte, J. Schwartz, On the role of pre-existing defects and magnetic flux avalanches in the degradation of $YBa_2Cu_3O_{7-x}$ coated conductors by quenching, Acta Mater. 60 (20) (2012) 6991–7000.

[5] C.L.H. Thieme, K.J. Gagnon, J.Y. Coulter, H. Song, J. Schwartz, Stability of second generation HTS pancake coils at 4.2 K for high heat flux applications, IEEE Trans. Appl. Supercond. 19 (3) (2009) 1626–1632.

[6] J. Schwartz, C.C. Koch, Y. Zhang, X. Liu, Formation of bismuth strontium calcium copper oxide superconductors, U.S. Patent US9773962B2, https://patentimages.storage.googleapis.com/dd/a0/5d/f73e3aa9c2eae4/US9773962.pdf, September 26, 2017.

[7] Y. Zhang, S. Johnson, G. Naderi, M. Chaubal, A. Hunt, J. Schwartz, High critical current density $Bi_2Sr_2CaCu_2O_x$/Ag wire containing oxide precursor synthesized from nano-oxides, Supercond. Sci. Technol. 29 (9) (2016) 095012.

[8] Y. Zhang, C.C. Koch, J. Schwartz, Formation of $Bi_2Sr_2CaCu_2O_x$/Ag multifilamentary metallic precursor powder-in-tube wires, Supercond. Sci. Technol. 29 (12) (2016) 125005.

[9] Y. Zhang, C.C. Koch, J. Schwartz, Synthesis of $Bi_2Sr_2CaCu_2O_x$ superconductors via direct oxidation of metallic precursors, Supercond. Sci. Technol. 27 (5) (2014) 055016.

[10] Y. Wang, J. Zheng, Z. Zhu, M. Zhang, W. Yuan, Quench behavior of high-temperature superconductor (RE) Ba2Cu3O × CORC cable, J. Phys. D, Appl. Phys. 52 (34) (2019) 345303.

[11] D. Qiu, W. Wu, Y. Pan, S. Xu, Z.M. Zhang, Z.L. Li, Z.Y. Li, Y. Wang, L. Wang, Y. Zhao, Z.W. Zhang, Experiment and numerical analysis on magnetic field stability of persistent current mode coil made of HTS-coated conductors, IEEE Trans. Appl. Supercond. 27 (4) (2017) 1–5.

[12] P. Yang, K. Li, Y. Wang, L. Wang, Q. Wu, A. Huang, Z. Hong, G. Jiang, Z. Jin, Quench protection system of a 1 MW high temperature superconductor DC induction heater, IEEE Trans. Appl. Supercond. 29 (5) (2019) 1–6.

[13] P. Yang, Y. Wang, D. Qiu, T. Chang, H. Ma, J. Zhu, Z. Jin, Z. Hong, Design and fabrication of a 1-MW high-temperature superconductor DC induction heater, IEEE Trans. Appl. Supercond. 28 (4) (2018) 1–5.

[14] Y. Pan, J. Sheng, W. Wu, Y. Wang, W. Zeng, Y. Zhao, Z.W. Zhang, Z. Li, Z. Hong, Z. Jin, Numerical study on simplified resistive joints of coated conductors: is there a lower limit of the joint resistance?, IEEE Trans. Appl. Supercond. 27 (4) (2017) 1–5.

[15] M. Li, Z. Wang, Y. Wang, J. Li, D. Viehland, Giant magnetoelectric effect in self-biased laminates under zero magnetic field, Appl. Phys. Lett. 102 (8) (2013) 082404.

[16] M. Li, C. Dong, H. Zhou, Z. Wang, X. Wang, X. Liang, Y. Lin, N.X. Sun, Highly sensitive DC magnetic field sensor based on nonlinear ME effect, IEEE Sens. Lett. 1 (6) (2017) 1–4.

[17] Y. Wang, D. Hasanyan, M. Li, J. Gao, J. Li, D. Viehland, Equivalent magnetic noise in multi-push-pull configuration magnetoelectric composites: model and experiment, IEEE Trans. Ultrason. Ferroelectr. Freq. Control 60 (6) (2013) 1227–1233.

[18] Y. Wang, D. Hasanyan, M. Li, J. Gao, R. Viswan, J. Li, D. Viehland, Magnetic field dependence of the effective permittivity in multiferroic composites, Phys. Status Solidi (a) 209 (10) (2012) 2059–2062.

[19] M. Li, D. Berry, J. Das, D. Gray, J. Li, D. Viehland, Enhanced sensitivity and reduced noise floor in magnetoelectric laminate sensors by an improved lamination process, J. Am. Ceram. Soc. 94 (11) (2011) 3738–3741.

[20] S.W. Cheong, M. Mostovoy, Multiferroics: a magnetic twist for ferroelectricity, Nat. Mater. 6 (1) (2007) 13–20.

[21] L. Lin, C. Gu, J. Zhu, Q. Ye, E. Jiang, W. Wang, M. Liao, Z. Yang, Y. Zeng, J. Sheng, W. Guo, Engineering of hole-selective contact for high-performance perovskite solar cell featuring silver back-electrode, J. Mater. Sci. 54 (10) (2019) 7789–7797.

[22] Z. Yang, Z. Liu, J. Sheng, W. Guo, Y. Zeng, P. Gao, J. Ye, Opto-electric investigation for Si/organic heterojunction single-nanowire solar cells, Sci. Rep. 7 (1) (2017) 1–9.

[23] W. Guo, R. Kirste, Z. Bryan, I. Bryan, M. Gerhold, R. Collazo, Z. Sitar, Nanostructure surface patterning of GaN thin films and application to AlGaN/AlN multiple quantum wells: a way towards light extraction efficiency enhancement of III-nitride based light emitting diodes, J. Appl. Phys. 117 (11) (2015) 113107.

[24] C. Li, X. Lu, W. Ding, L. Feng, Y. Gao, Z. Guo, Formability of ABX_3 ($X =$ F, Cl, Br, I) halide perovskites, Acta Crystallogr., Sect. B, Struct. Sci. 64 (6) (2008) 702–707.

[25] A.S. Verma, V.K. Jindal, Lattice constant of cubic perovskites, J. Alloys Compd. 485 (1–2) (2009) 514–518.

[26] Y. Zhang, X. Xu, Yttrium barium copper oxide superconducting transition temperature modeling through Gaussian process regression, Comput. Mater. Sci. 179 (2020) 109583.

[27] Y. Zhang, X. Xu, Predicting doped MgB_2 superconductor critical temperature from lattice parameters using Gaussian process regression, Physica C, Supercond. Appl. 573 (2020) 1353633.

[28] Y. Zhang, X. Xu, Curie temperature modeling of magnetocaloric lanthanum manganites using Gaussian process regression, J. Magn. Magn. Mater. 512 (2020) 166998.

[29] Y. Zhang, X. Xu, Machine learning the magnetocaloric effect in manganites from lattice parameters, Appl. Phys. A 126 (2020) 341.

[30] Y. Zhang, X. Xu, Machine learning the magnetocaloric effect in manganites from compositions and structural parameters, AIP Adv. 10 (3) (2020) 035220.

[31] Y. Zhang, X. Xu, Predicting the thermal conductivity enhancement of nanofluids using computational intelligence, Phys. Lett. A 384 (2020) 126500.

[32] Y. Zhang, X. Xu, Machine learning modeling of lattice constants for half-Heusler alloys, AIP Adv. 10 (2020) 045121.

[33] Y. Zhang, X. Xu, Machine learning optical band gaps of doped-ZnO films, Optik 217 (2020) 164808.

[34] Y. Zhang, X. Xu, Relative cooling power modeling of lanthanum manganites using Gaussian process regression, RSC Adv. 10 (2020) 20646–20653.

[35] Y. Zhang, X. Xu, Machine learning band gaps of doped-TiO_2 photocatalysts from structural and morphological parameters, ACS Omega 5 (2020) 15344–15352.

[36] Y. Zhang, X. Xu, Machine learning lattice constants for cubic perovskite $A_2^{2+}BB'O_6$ compounds, CrystEngComm 22 (2020) 6385–6397.

[37] Y. Zhang, X. Xu, Machine learning lattice constants for cubic perovskite ABX_3 compounds, ChemistrySelect 5 (2020) 9999–10009.

[38] Y. Zhang, X. Xu, Predicting As_xSe_{1-x} glass transition onset temperature, Int. J. Thermophys. 41 (2020) 149.

[39] Y. Zhang, X. Xu, Lattice misfit predictions via the Gaussian process regression for Ni-based single crystal superalloys, Met. Mater. Int. 27 (2) (2021) 235–253.

[40] Y. Zhang, X. Xu, Machine learning lattice constants from ionic radii and electronegativities for cubic perovskite A_2XY_6 compounds, Phys. Chem. Miner. 47 (2020) 39.

[41] Y. Zhang, X. Xu, Transformation temperature predictions through computational intelligence for NiTi-based shape memory alloys, Shape Mem. Superelast. 6 (2020) 374–386.

[42] Y. Zhang, X. Xu, Machine learning lattice parameters of monoclinic double perovskites, Int. J. Quant. Chem. 121 (5) (2021) e26480.

[43] Y. Zhang, X. Xu, Fe-based superconducting transition temperature modeling through Gaussian process regression, J. Low Temp. Phys. 202 (2021) 205–218.

[44] Y. Zhang, X. Xu, Machine learning decomposition onset temperature of lubricant additives, J. Mater. Eng. Perform. 29 (2020) 6605–6616.

[45] Y. Zhang, X. Xu, Predicting doped Fe-based superconductor critical temperature from structural and topological parameters using machine learning, Int. J. Mater. Res. 112 (1) (2021) 2–9.

[46] Y. Zhang, X. Xu, Machine learning glass transition temperature of polymers, Heliyon 6 (2020) e05055.

[47] Y. Zhang, X. Xu, Machine learning F-doped Bi(Pb)–Sr–Ca–Cu–O superconducting transition temperature, J. Supercond. Nov. Magn. 34 (1) (2021) 63–73.

[48] Y. Zhang, X. Xu, Machine learning the central magnetic flux density of superconducting solenoids, Mater. Technol. (2020).

[49] Y. Zhang, X. Xu, Machine learning lattice constants for spinel compounds, Chem. Phys. Lett. 760 (2020) 137993.

[50] Y. Zhang, X. Xu, Solubility predictions through LSBoost for supercritical carbon dioxide in ionic liquids, New J. Chem. 44 (2020) 20544–20567.

[51] L.Q. Jiang, J.K. Guo, H.B. Liu, M. Zhu, X. Zhou, P. Wu, C.H. Li, Prediction of lattice constant in cubic perovskites, J. Phys. Chem. Solids 67 (7) (2006) 1531–1536.

[52] Y. Li, W. Yang, R. Dong, J. Hu, MLatticeABC: generic lattice constant prediction of crystal materials using machine learning, arXiv preprint, arXiv:2010.16099, 2020.

[53] R.L. Moreira, A. Dias, Comment on 'Prediction of lattice constant in cubic perovskites', J. Phys. Chem. Solids 68 (8) (2007) 1617–1622.

[54] R.D. Shannon, Revised effective ionic radii and systematic studies of interatomic distances in halides and chalcogenides, Acta Crystallogr., Sect. A Cryst. Phys. Diffr. Theor. Gen. Crystallogr. 32 (5) (1976) 751–767.

[55] J.M. Albina, M. Mrovec, B. Meyer, C. Elsässer, Structure, stability, and electronic properties of $SrTiO_3/LaAlO_3$ and $SrTiO_3/SrRuO_3$ interfaces, Phys. Rev. B 76 (16) (2007) 165103.

[56] H. Wang, B. Wang, Q. Li, Z. Zhu, R. Wang, C.H. Woo, First-principles study of the cubic perovskites $BiMO_3$ ($M =$ Al, Ga, In, and Sc), Phys. Rev. B 75 (24) (2007) 245209.

[57] C. Li, B. Wang, R. Wang, H. Wang, X. Lu, First-principles study of structural, elastic, electronic, and optical properties of orthorhombic $BiGaO_3$, Comput. Mater. Sci. 42 (4) (2008) 614–618.

[58] G.A. Geguzina, V.P. Sakhnenko, Correlation between the lattice parameters of crystals with perovskite structure, Crystallogr. Rep. 49 (1) (2004) 15–19.